Electronic Supplementary Information

Unmasking Active Sites in Linker Coordinated Nickel-Cobalt Hydroxide for Electrocatalytic Iodide Oxidation Reaction

Ayusie Goyal,[a] Trinh Hai Binh,[b] Labham Singh,[a] Pragya Arora,[a] Anamika Yadav,[a] Chung-Li Dong,[b]* Baghendra Singh,[a]* Apparao Draksharapu[a]*

[a]Southern Laboratories-208A, Department of Chemistry, Indian Institute of Technology Kanpur, Kanpur-208016, India
E-mail: baghendras@iitk.ac.in, appud@iitk.ac.in
[b]Department of Physics, Tamkang University, New Taipei City, Taiwan
E-mail: cldong@mail.tku.edu.tw

Experimental section

Chemicals

All the chemicals employed for catalyst preparation were of analytical grade and used without any prior purification. Nickel foam was acquired from D. Tech Solutions Pvt. Ltd., Kanpur, India. Throughout the synthesis and electrochemical studies, double-distilled water was used. Nickel(II) nitrate hexahydrate [$Ni(NO_3)_2.6H_2O$, 98%] and cobalt(II) acetate tetrahydrate [$Co(OAc)_2.4H_2O$, 99%] were sourced from SRL Chemicals, while sodium benzoate ($C_7H_5NaO_2$, 98%) was purchased from TCI. Potassium iodide (KI, 98%)was purchased from Rankem Pvt. Ltd.

Activation of Nickel foam[1]

Nickel foam (NF) strips (1 cm × 2 cm) were first cleaned using acetone, followed by thorough rinsing with distilled water. Subsequently, NF stripes were sonicated in 1.0 M HCl for 15 minutes, washed again with distilled water, and dried in an oven at 50 ^oC for 12 h.

Synthesis of NiCo-H

The NiCo-H was synthesised by a simple hydrothermal method. Firstly, a solution of 50 mM of $Co(OAc)_2.4H_2O$ and 50 mM of $Ni(NO_3)_2.6H_2O$ was prepared in 11 mL of distilled water. After that, the prepared solution was poured into a 20 mL Teflon-lined autoclave, and activated NF strips were placed vertically in the solution. The sealed autoclave was heated at 120 °C for 6 h in an air oven. After natural cooling at room temperature, NiCo-H coated on NF were collected from the autoclave and washed with water and ethanol several times, followed by drying at 60 ^oC for overnight.

Synthesis of BZ-NiCo-H

The BZ-NiCo-H catalyst was synthesised by a step hydrothermal method. A solution of 50 mM of $Co(OAc)_2.4H_2O$, 50 mM of $Ni(NO_3)_2.6H_2O$, and 50 mM $C_7H_5NaO_2$ was prepared in 11 mL of distilled water. The prepared solution was poured into a 20 mL Teflon-lined autoclave, and activated NF stripes were placed vertically in the solution. The sealed autoclave was heated at 120 °C for 6 h in an air oven. After naturally cooling to room temperature, the BZ-NiCo-H coated on NF were collected, thoroughly washed with deionized water and ethanol several times, and then dried at 60 °C overnight.

Characterization

The phase composition and crystallinity of the prepared catalysts were investigated using powder X-ray diffraction (PXRD), performed on a PANalytical X'Pert diffractometer operated with Cu Kα radiation (λ = 0.154 nm). Diffraction patterns were recorded over a 2θ range of 05°-60°, employing a step size of 0.01°. The X-ray photoelectron spectroscopy (XPS) was used for the analysis of the

oxidation state of the elements present in the catalyst, using a PHI 5000 VersaProbe II instrument. Origin Pro 8.5 software was used for XPS data fitting. The morphology and microstructural aspects of the surface were examined using a JEOL JSM-6010LA tungsten-electron microscope (W-SEM). Energy-dispersive X-ray spectroscopy (EDX) was used to determine the elemental composition. Additionally, high-resolution imaging was performed using a Tecnai G2 20 TWIN transmission electron microscope (TEM).

X-ray absorption spectroscopy (XAS) measurements using synchrotron radiation were carried out at beamline BL17C of the Taiwan Light Source (TLS), housed at the National Synchrotron Radiation Research Center (NSRRC), Taiwan. The beamline employs a Si (111) double-crystal monochromator, with the TLS storage ring functioning at 1.5 GeV and a typical current of around 360 mA. X-ray absorption spectroscopy (XAS) comprises two primary regions: The X-ray absorption near-edge structure (XANES) and the extended X-ray absorption fine structure (EXAFS). XANES, typically spanning from ~30 eV below to ~100 eV above the absorption edge, offers valuable information regarding the oxidation state and electronic band occupancy, as it corresponds to the binding energies of core-level electrons. The extended X-ray absorption fine structure (EXAFS) region, typically ranging from ~50 eV to 1000 eV above the absorption edge, provides detailed insights into the local atomic environment, including coordination numbers, interatomic distances, and structural disorder (Debye–Waller factors). For measurements at the Ni and Co K-edges, an energy resolution of 0.35 eV was employed, and all spectra were acquired in transmission mode. Data processing involved standard procedures such as background subtraction, edge normalization, and Fourier transformation.

Electrochemical measurements

Electrochemical evaluations were performed using a typical three-electrode arrangement, with 1.0 M KOH solution serving as the electrolyte. The synthesized materials were used as the working electrode in a three-electrode setup, with Hg/HgO serving as the reference electrode and platinum wire as the counter electrode. The oxygen evolution reaction (OER) activity was carried out in 1.0 M KOH solution. To investigate the iodide oxidation reaction (IOR), 0.33 M KI was added to the 1.0 M KOH electrolyte. Cyclic voltammetry (CV) and linear sweep voltammetry (LSV) measurements were performed with 100% iR drop correction applied (scan rate 5 mV s^{-1}). Electrode potentials were referenced to the reversible hydrogen electrode (RHE) using the equation:

$$E(RHE) = E(Hg/HgO) + 0.098 + 0.059\ pH$$

Electrochemical impedance spectroscopy (EIS) was conducted over a frequency range of 0.01 to 10,00,000 Hz with an amplitude of 10 mV. The charge transfer resistance (R_{ct}) was determined from the semicircle diameters observed in the Nyquist plots. Chronoamperometric measurements (CA) were conducted at a fixed potential and reported without iR compensation. To determine the double-

layer capacitance (C_{dl}), cyclic voltammetry (CV) was conducted within a potential range that excluded any prominent faradaic reactions. In the two-electrode H-type electrochemical setup, the catalyst was employed at both anode and cathode to evaluate the performance for paired electrolysis.

Determination of Faradaic efficiency and yield rate

The yield rate for iodate production has been calculated using the following formula:

$$\mathbf{YR_P = (C_P \times V) / (t \times A)}$$

where YR_P is the yield rate of the product (mmol cm^{-2} h^{-1}), C_P is the concentration of product in the electrolyte (mmol L^{-1}), V is the volume of electrolyte (L), t is the electrolysis time (h), and A is the geometrical surface area of the working electrode (1 cm^2).

Faradaic efficiency for iodate production has been determined by using the following formula:

$$\mathbf{FE\ (\%) = (n \times F \times C_n) / Q \times 100}$$

where FE denotes the faradaic efficiency of the reaction, n is the number of electrons transferred during the reaction, F is the Faraday's constant (96485 C mol^{-1}), C_n is the concentration of product in the electrolyte (mmol), and Q is the total charge passing the electrode.

Determination of iodate

Resonance Raman spectroscopy was employed to analyze iodate in the electrolyte, which displayed a distinct vibrational band at 800 cm^{-1}. The resonance Raman spectra were acquired using a 473 nm laser (80 mW, Cobolt lasers, HÜBNER Photonics). The spectra of the electrolytes were recorded using distinct excitation wavelengths and instrument settings. The measurements were conducted using a Kymera 328i motorized Czerny-Turner spectrograph (Andor Technology), coupled with a DU 420 A-BEX2-DD CCD detector (iDus 420, Andor Technology), thermoelectrically cooled to −80 °C to reduce noise. A slit width of 100 µm was used to achieve the desired spectral resolution. The spectral calibration was carried out using a 1:1 (v/v) mixture of acetonitrile and toluene. To quantify iodate concentration, a calibration curve was obtained from different iodate solutions (50 mM, 100 mM, 150 mM, 200 mM, 250 mM, and 300 mM) prepared in 100 mM Na_2SO_4.

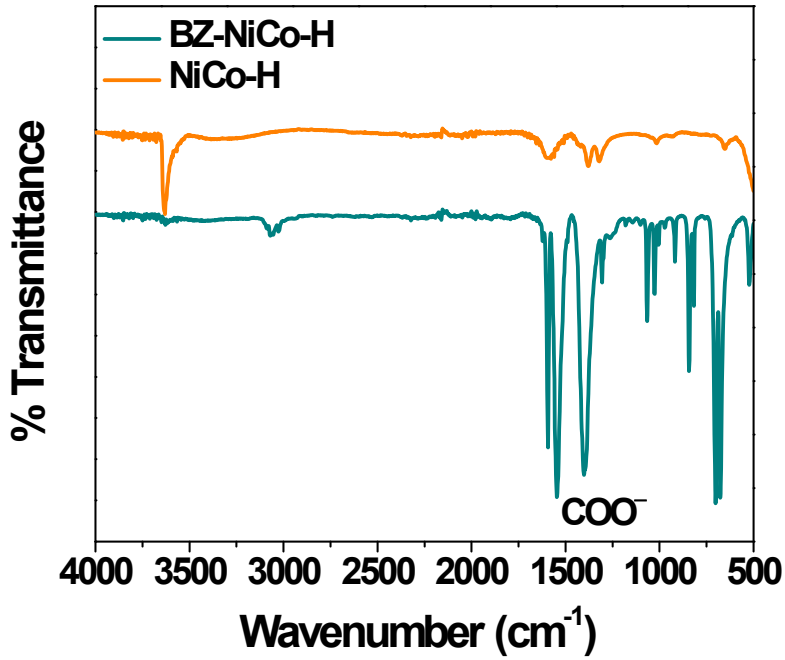

Figure S1. IR spectra of NiCo-H and BZ-NiCo-H showing the characteristic peaks.[2,3]

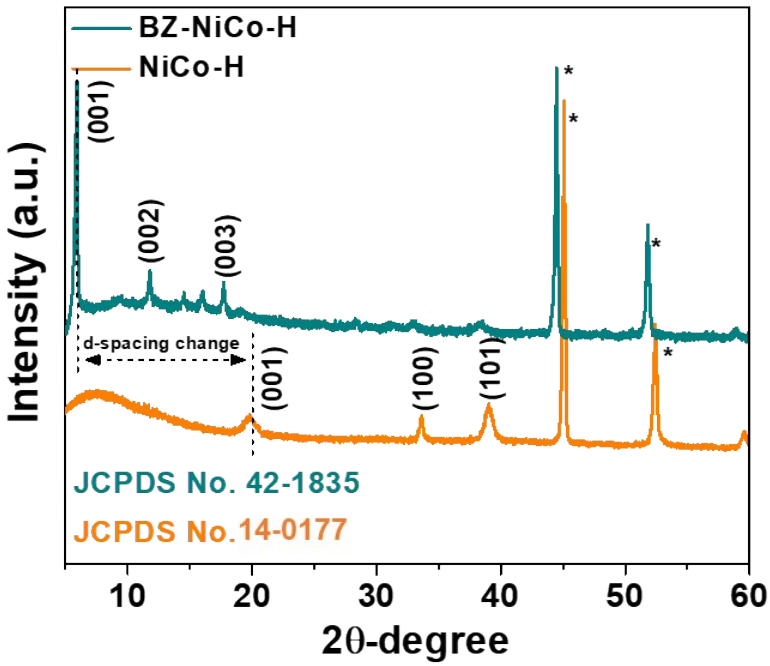

Figure S2. PXRD data showing the peaks for the $Ni(OH)(C_6H_5COO).H_2O$ phase (JCPDS No. 42-1835) and β-$Ni(OH)_2$ phase (JCPDS No. 14-0177) of BZ-NiCo-H and NiCo-H, respectively, (* peaks are assigned for Ni foam).

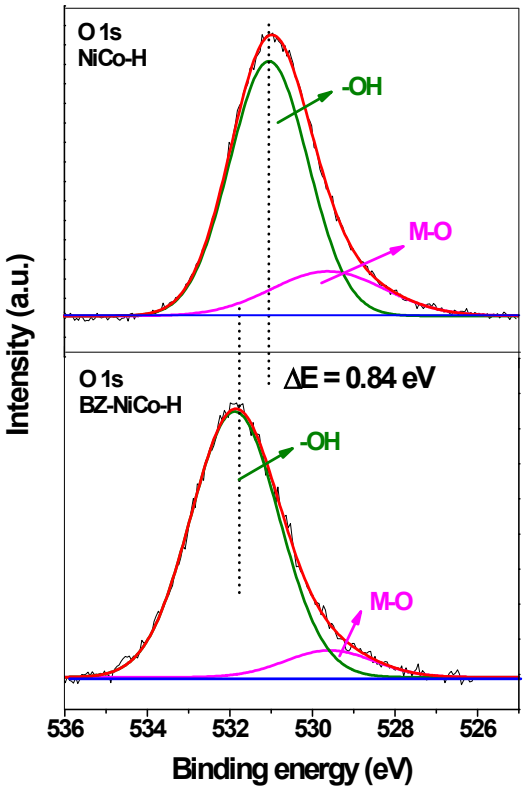

Figure S3. O 1s XPS data of NiCo-H and BZ-NiCo-H, showing two signals for metal-oxygen bond and surface hydroxyl groups. The -OH peak in NiCo-H showed a negative shift of 0.84 eV compared to BZ-NiCo-H.[4]

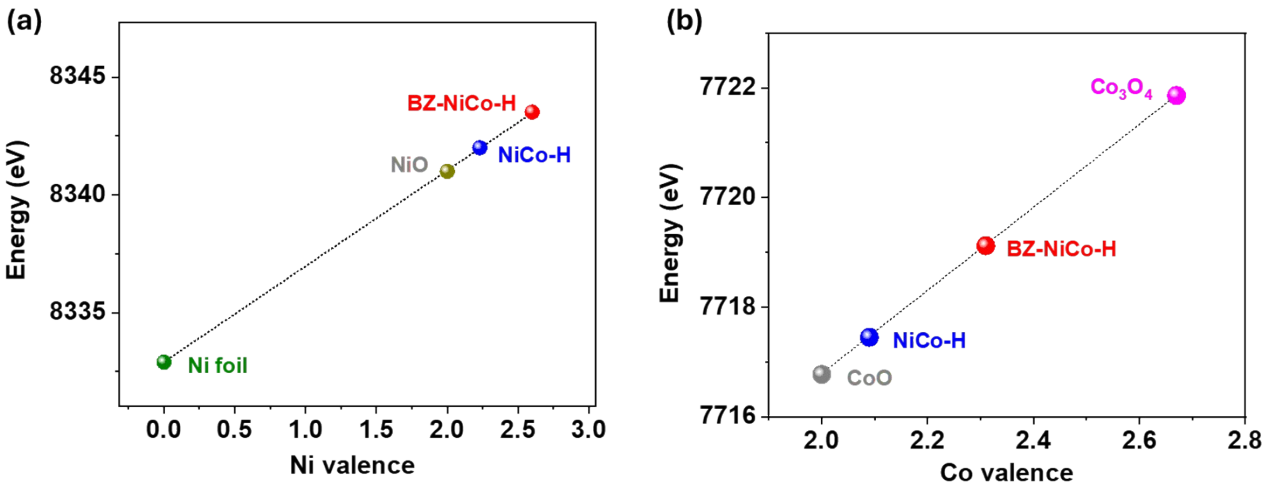

Figure S4. (a) Average oxidation state of Ni in BZ-NiCo-H and NiCo-H; and (b) average oxidation state of Co in BZ-NiCo-H and NiCo-H.

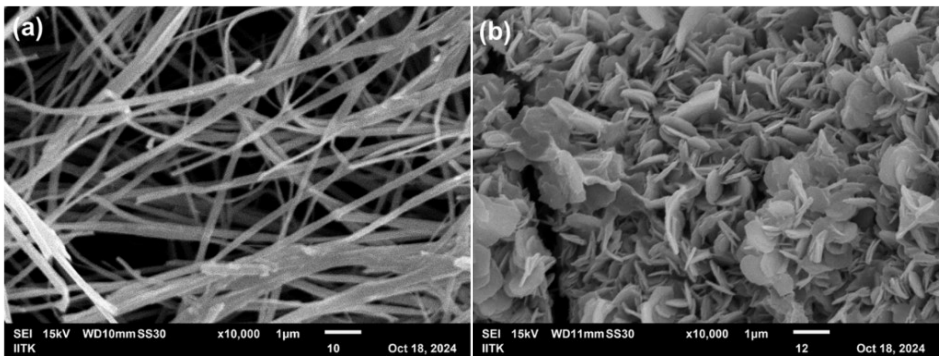

Figure S5. (a) SEM image of BZ-NiCo-H showing nanowires, and (b) SEM image of NiCo-H indicating nanosheet morphology.

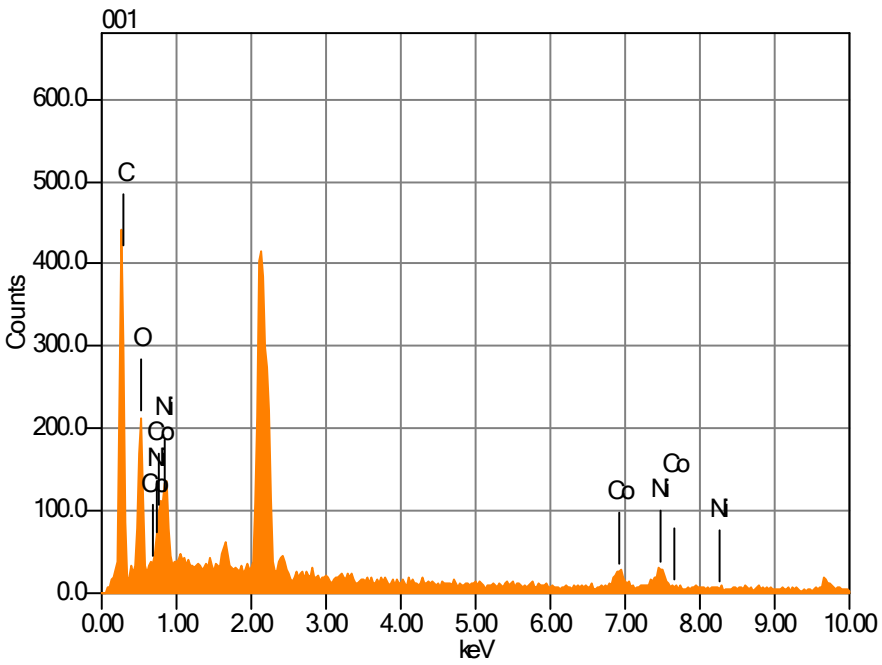

Figure S6. EDX spectrum of BZ-NiCo-H showing the existence of Ni, Co, C, and O elements.

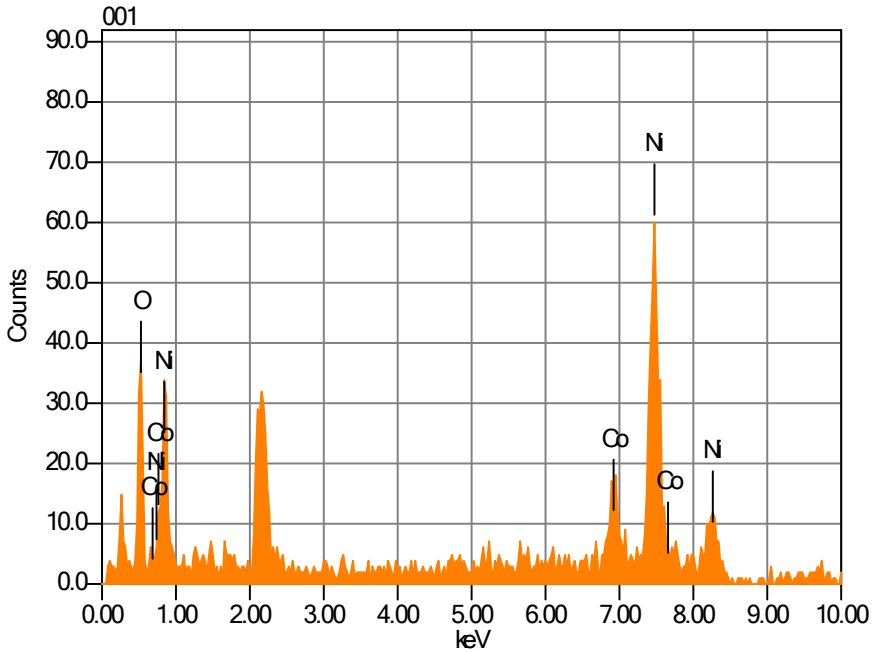

Figure S7. EDX spectrum of NiCo-H showing the existence of Ni, Co, and O elements.

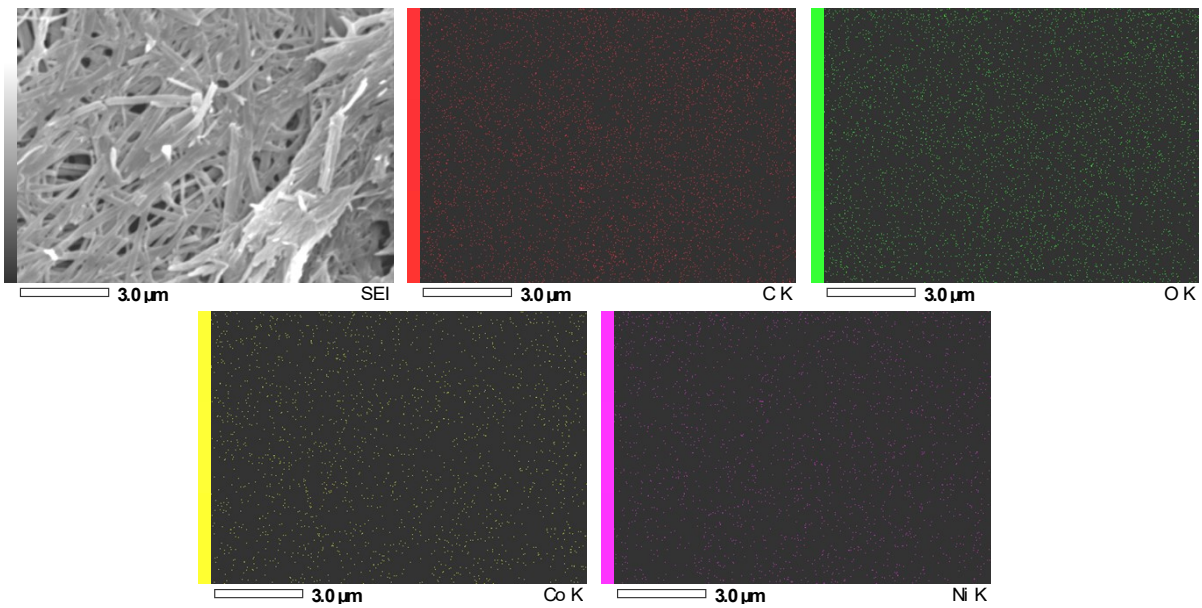

Figure S8. Elemental mapping images of BZ-NiCo-H showing the uniform distribution of Ni, Co, C, and O elements.

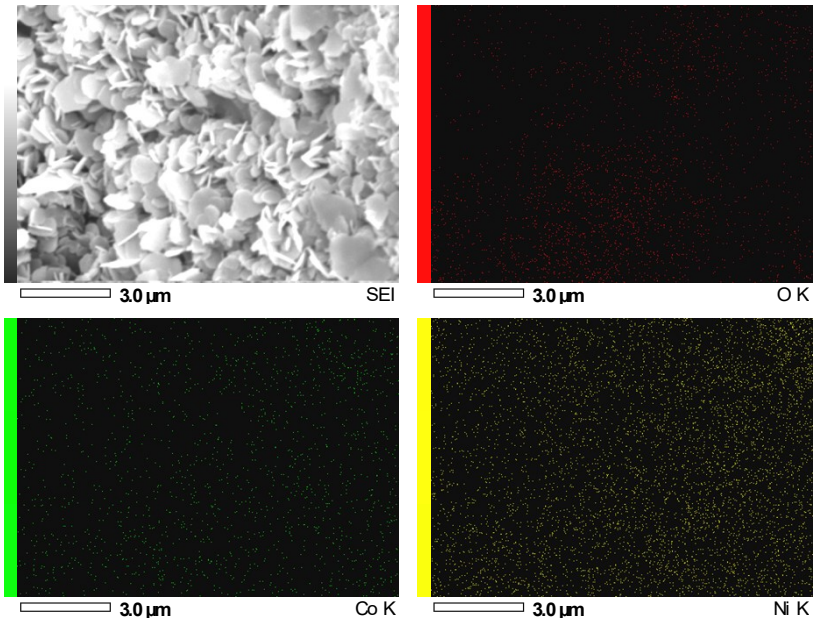

Figure S9. Elemental mapping images of NiCo-H showing the uniform distribution of Ni, Co, and O elements.

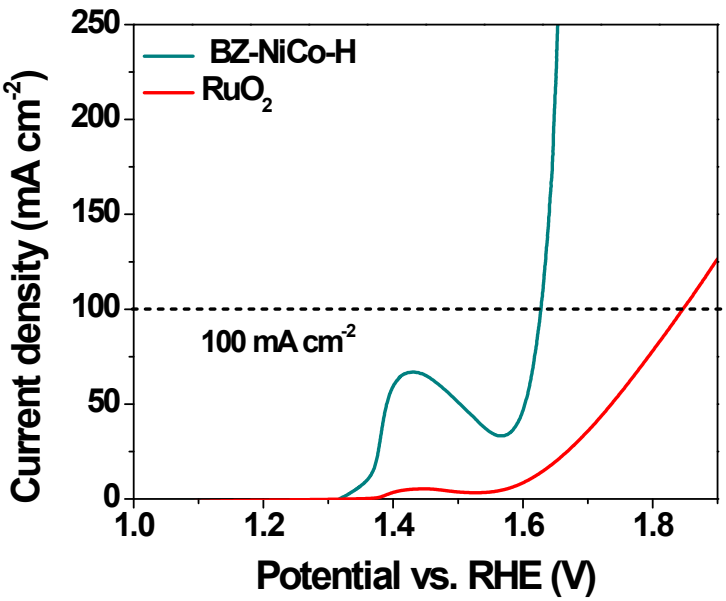

Figure S10. Comparison of OER activity of BZ-NiCo-H and RuO_2.

Table S1: Comparison of OER activity of BZ-NiCo-H with some literature-reported catalysts.

Catalyst	Electrolyte	Overpotential (mV)	Current density (mA cm^{-2})	References
BZ-NiCo-H	*1 M KOH*	*400*	*100*	***This work***
NiCo-LDH/GO-CNTs	0.1 M KOH	290	10	*Nano Res.*, 2021, **14**, *4783-4788*
CQD/NiCo-LDH	1 M KOH	266	10	*J. Mater. Sci. Mater. Electron,* 2024, **35**, 1037
NiCo-LDH/CoP/NF	1 M KOH	253	10	*Inorg. Chem. Commun.*, 2023, **157**, 111347
Mo- $BaNiS_2$	1 M KOH	214	10	*J. Indian Chem. Soc.*, 2025, **102**, 101788
$CuFe_2O_4$/PANI	1 M KOH	218	10	*J. Indian Chem. Soc.*, 2025, **102**, 101759
Ni_3S_2@Mo-CoFe LDH	1 M KOH	233	50	*J. Electroanal. Chem.*, 2025, **979**, 118931
NC@CeO_2-CoFe	1 M KOH	255	10	*Sep. Purif. Technol.*, 2025, **362**, 131699
CoFe/$CoFe_2O_4$@NC	1 M KOH	330	50	*Chem. Eng. J.*, 2025, **523**, 168363
MoS_2/CoFe-LDH/NF	1 M KOH	255	50	*ACS Appl. Nano Mater.*, 2025, **8**, 12717-12726
CoFe-MOF/CNTs/rGO	1 M KOH	253	10	*ACS Appl. Nano Mater.*, 2025, **8**, 13552–13562
CuS–CuO@NiFe-LDH	1 M KOH	285	10	*New J. Chem.*, 2025, **49**, 10832-10840
NiFe-LDH/Co/C@NF	1 M KOH	244	50	*Solid State Commun.*, 2025, **401**, 115939
Co_3O_4/$NiFe_2O_4$	1 M KOH	236	10	*Dalton Trans.*, 2025, **54**, 13110-13117
NiFeCo	1 M KOH	234	10	*ChemCatChem*, 2025, **17**, e00454

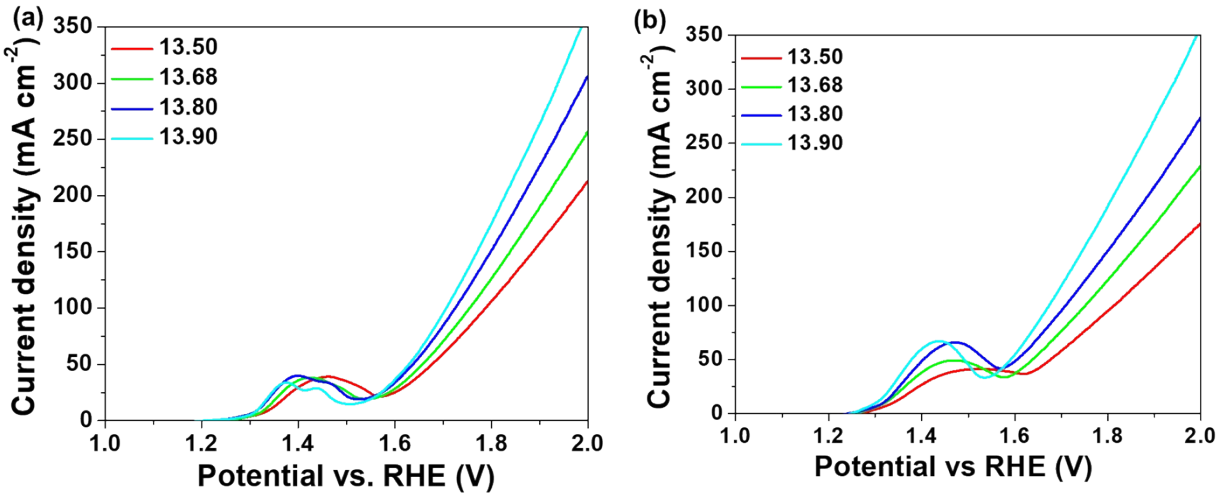

Figure S11. pH-dependent OER activity of (a) NiCo-H, and (b) BZ-NiCo-H, showing minimum sensitivity of NiCo-H towards pH change compared to BZ-NiCo-H.[5]

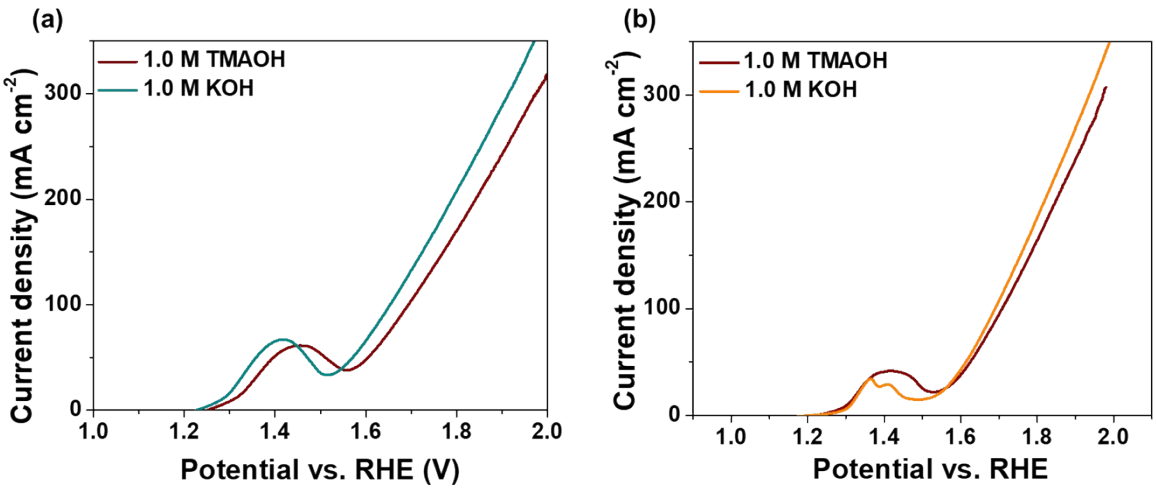

Figure S12. OER activity of (a) BZ-NiCo-H and (b) NiCo-H in 1.0 M KOH and 1.0 M TMAOH.[5]

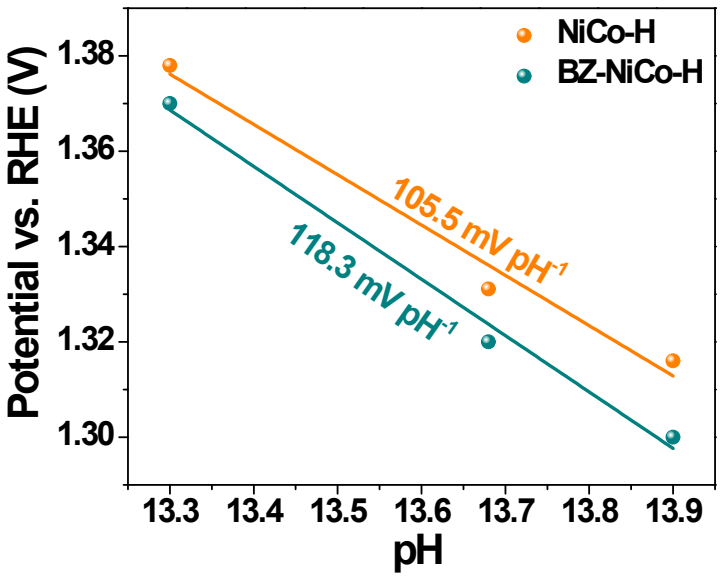

Figure S13. Pourbaix diagram for potential against pH at 10 mA cm^{-2} current density for the synthesized catalysts BZ-NiCo-H and NiCo-H.[5]

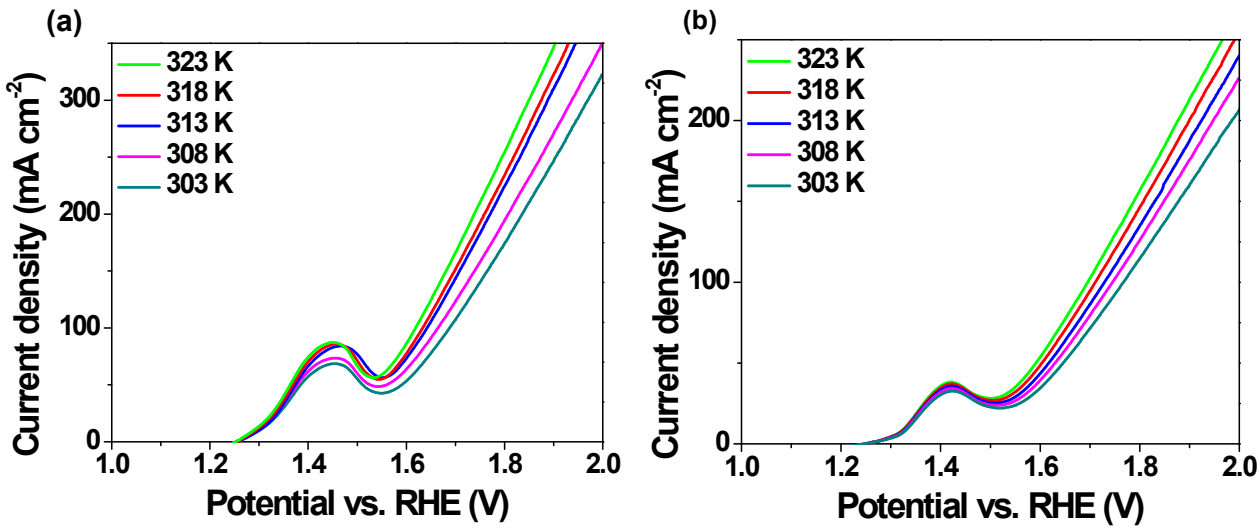

Figure S14. Temperature-dependent OER-LSVs of (a) BZ-NiCo-H and (b) NiCo-H in 1.0 M KOH.[5]

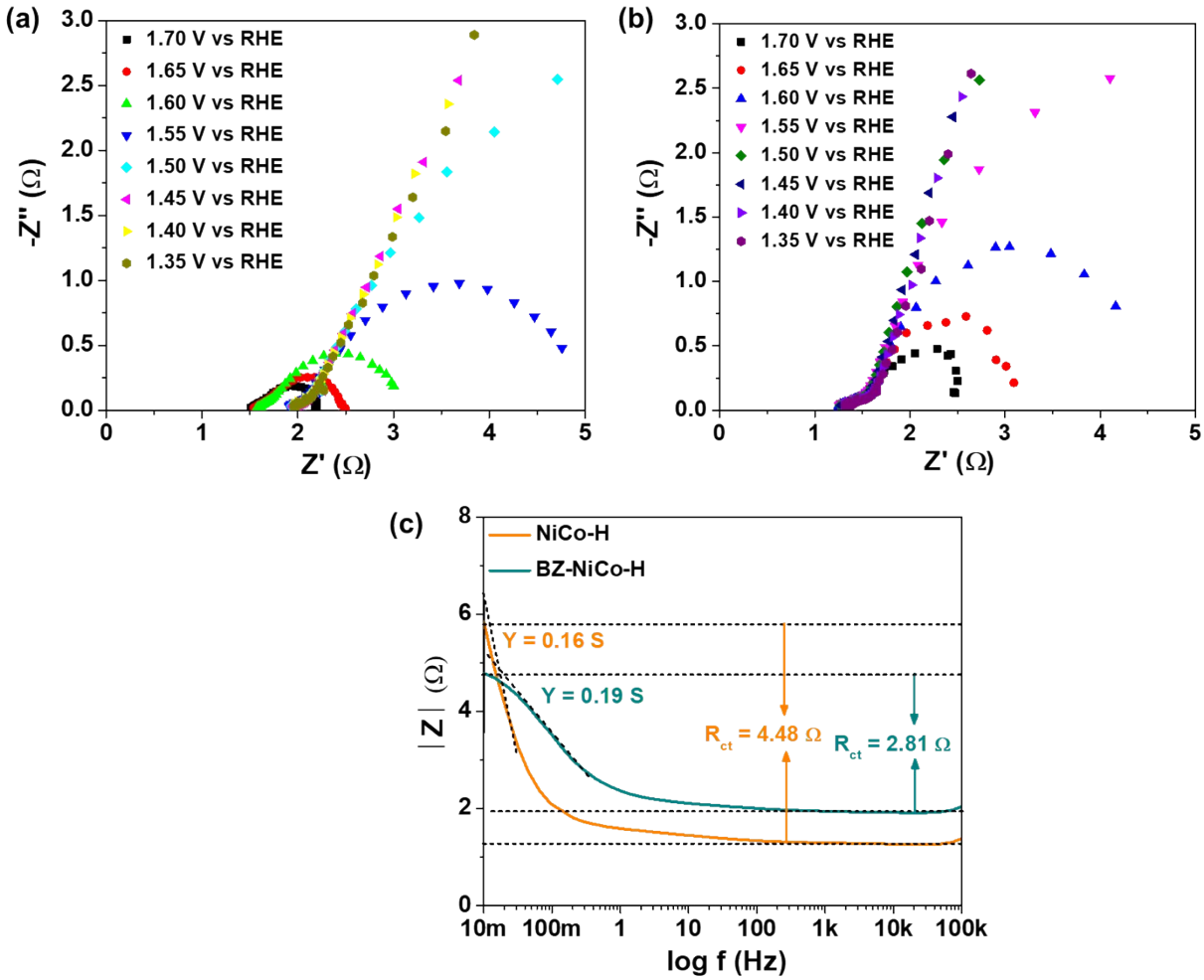

Figure S15. (a) Nyquist plots of BZ-NiCo-H at different potentials for OER, (b) Nyquist plots of NiCo-H at different potentials for OER, and (c) Bode absolute impedance plot of BZ-NiCo-H and NiCo-H.[6]

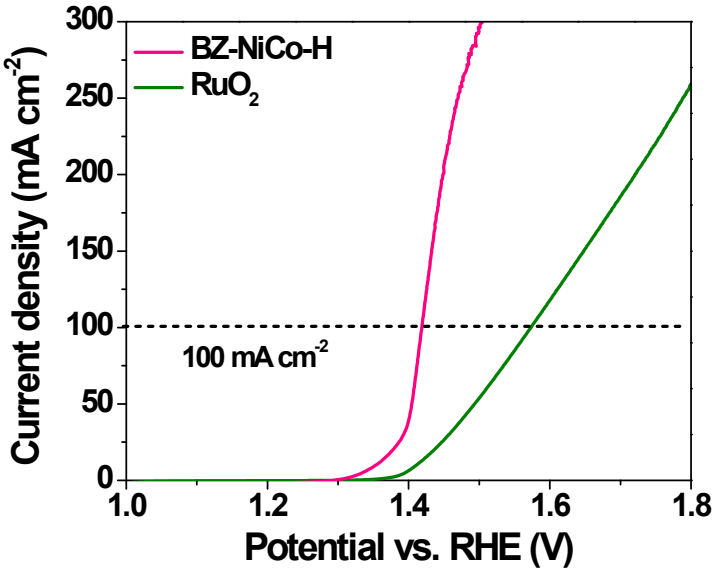

Figure S16. Comparison of IOR activity of BZ-NiCo-H and RuO_2.

Table S2: Comparison of IOR activity of BZ-NiCo-H with some literature-reported catalysts.

Catalysts	Electrolyte	Potential (V vs RHE)	Current density (mA cm^{-2})	Reference
BZ-NiCo-H	*1 M KOH + 0.33 M KI*	*1.42*	*100*	***This work***
NiCo-H	*1 M KOH + 0.33 M KI*	*1.48*	*100*	***This wok***
RuTiO-550	0.1 M $HClO_4$ + 0.1 M NaI	1.01	10	*Appl. Catal., B*, 2022, **316**, 121608
RuSn SAO	0.1 M $HClO_4$ + 0.1 M NaI	1.01	10	*ACS Sustainable Chem. Eng.*, 2021, **9**, 8803-8812
Mo-N_4/d-C	0.1 M KOH + 0.1 M NaI	0.94	10	*Nano Lett.*, 2022, **22**, 7311-7317
Carbon fiber paper (CFP)	0.1 M $HClO_4$ + 0.1 M NaI	0.55	10	*J. Mater. Chem. A*, 2022, **10**, 23982-23989
Ni-$Co(OH)_2$ NSAs	1 M KOH + 0.33 M KI	1.32	50	*Nanoscale Adv.*, 2021, **3**, 604-610
$Co(OH)_2$ NSAs	1 M KOH + 0.33 M KI	1.33	50	*Nanoscale Adv.*, 2021, **3**, 604-610
Pt/Co_3O_4	1 M KOH + 0.8 M KI	1.29	20	*Energy Storage Mater.*, 2024, **73**, 103817
MoS_2-FeS_2	1 M$HClO_4$ + 0.5 M NaI	0.52	10	*ACS Appl. Energy Mater.*, 2024, **7**, 2653-2664

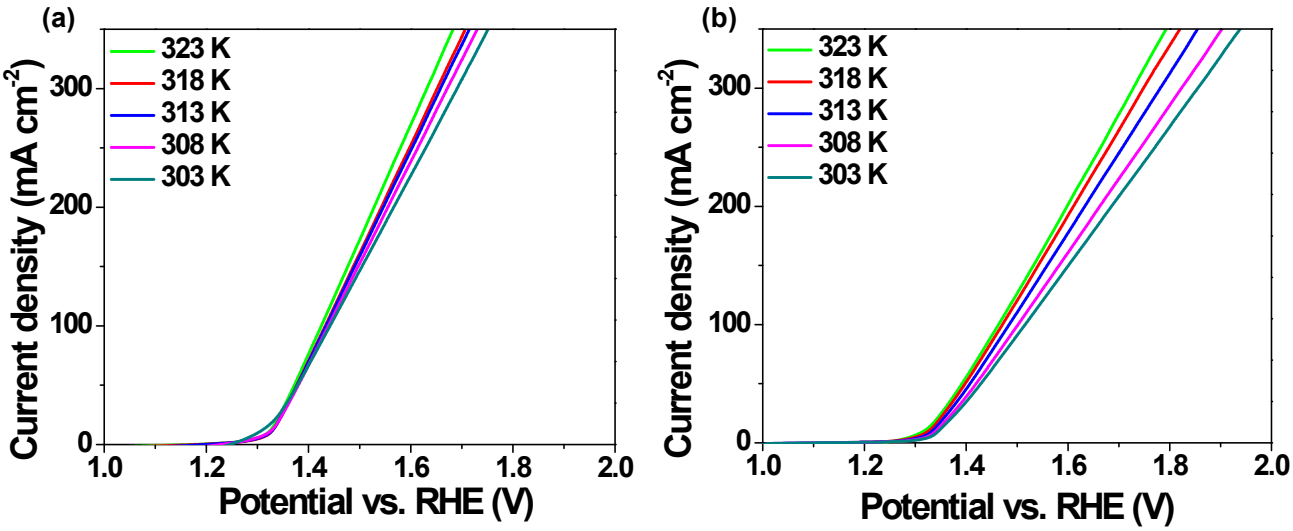

Figure S17. (a) Temperature-dependent IOR-LSVs of BZ-NiCo-H in 1.0 M KOH + 0.33 M KI, and (b) temperature-dependent IOR-LSVs of NiCo-H in 1.0 M KOH + 0.33 M KI.[6]

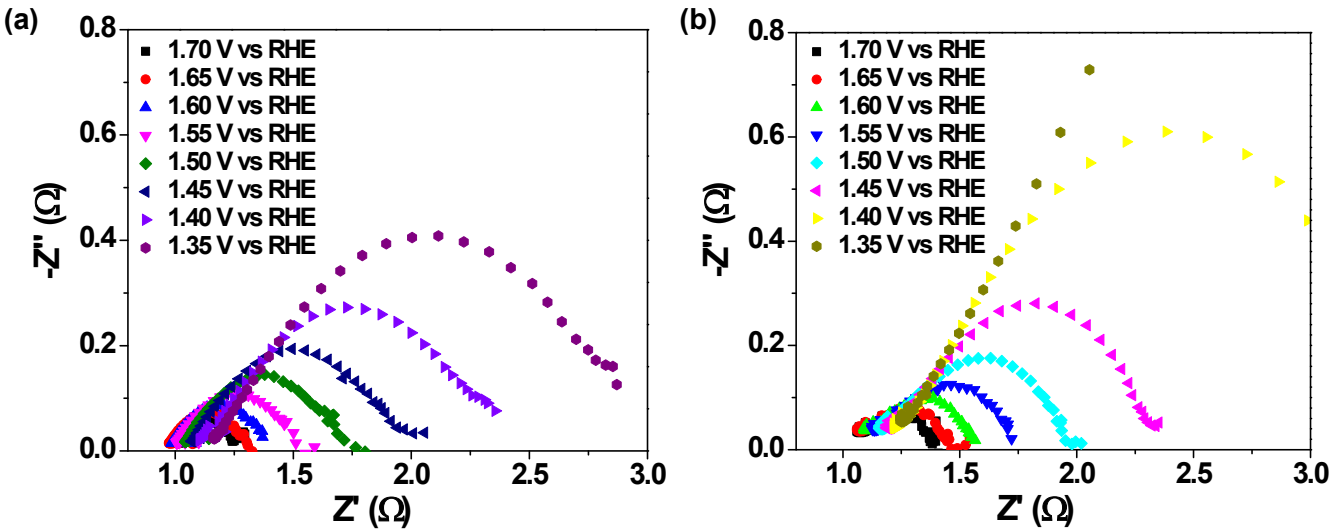

Figure S18. Nyquist plots of (a) BZ-NiCo-H and (b) NiCo-H at different potentials for IOR.[6]

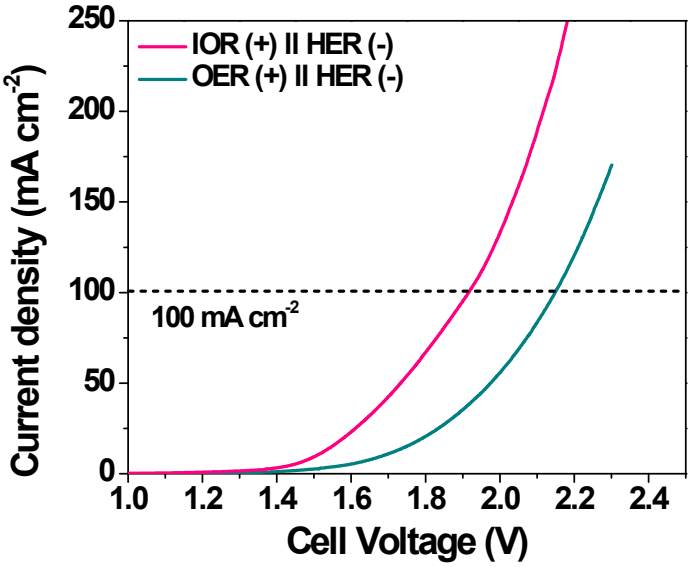

Figure S19. LSV profiles for overall water electrolysis and IOR-assisted water electrolysis in a two-electrode system using BZ-NiCo-H catalysts.

For OER:

Energy required = Voltage (V) x Current (mA) / H_2 production rate (L/h)

= 2.15 x 100 / 0.0438 = 4908 Wh m^{-3} H_2 = 4.90 kWh m^{-3} H_2

For IOR:

Energy required = Voltage (V) x Current (mA) / H_2 production rate (L/h)

= 1.92 x 100 / 0.0956 = 2008 Wh m^{-3} H_2 = 2.08 kWh m^{-3} H_2

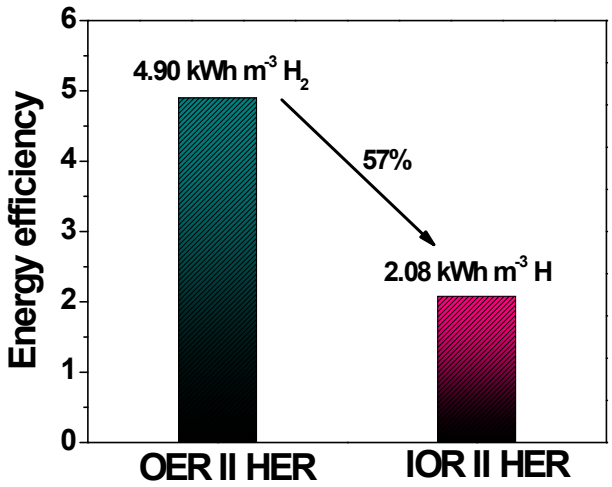

Figure S20. Energy consumption during OER/HER and IOR/HER in a two-electrode system (H-cell) using BZ-NiCo-H.[7]

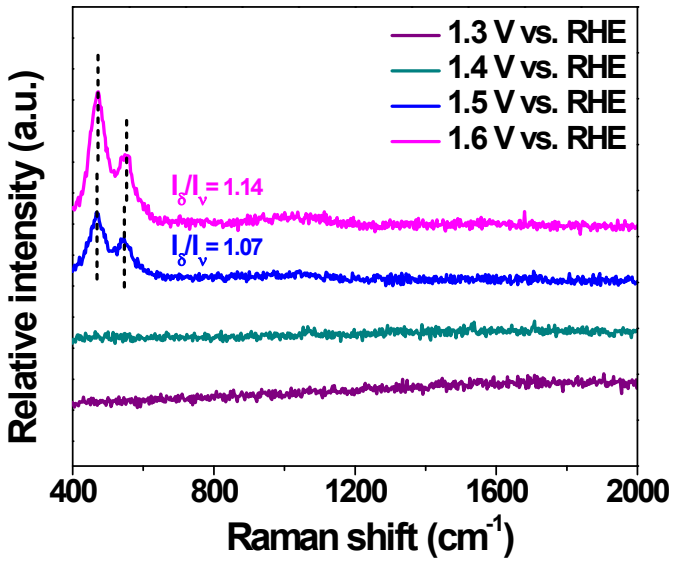

Figure S21. In-situ Raman data of NiCo-H for OER under applied anodic potentials.

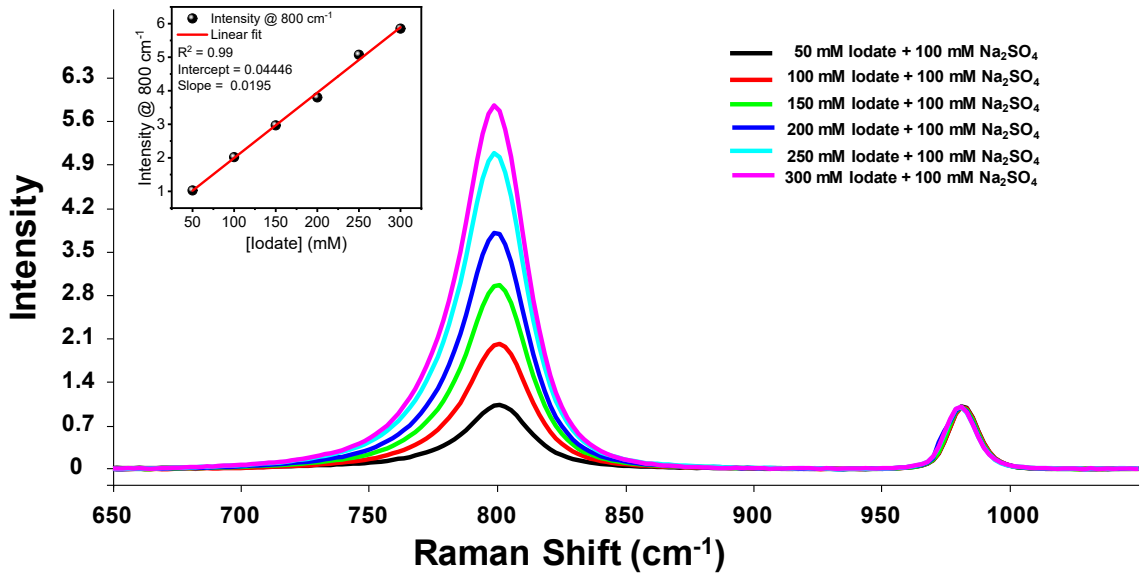

Figure S22. Raman spectra and calibration plot of iodate at different concentrations. The calibration for the resonance enhanced band for iodate has been made by recording with different concentrations of iodate ion (50, 100,150, 200, 250, and 300 mM) and the same concentration of sodium sulphate (100 mM) using a 473 nm Laser. We calibrated the iodate intensity with respect to the sodium sulphate signal at 980 cm^{-1}.

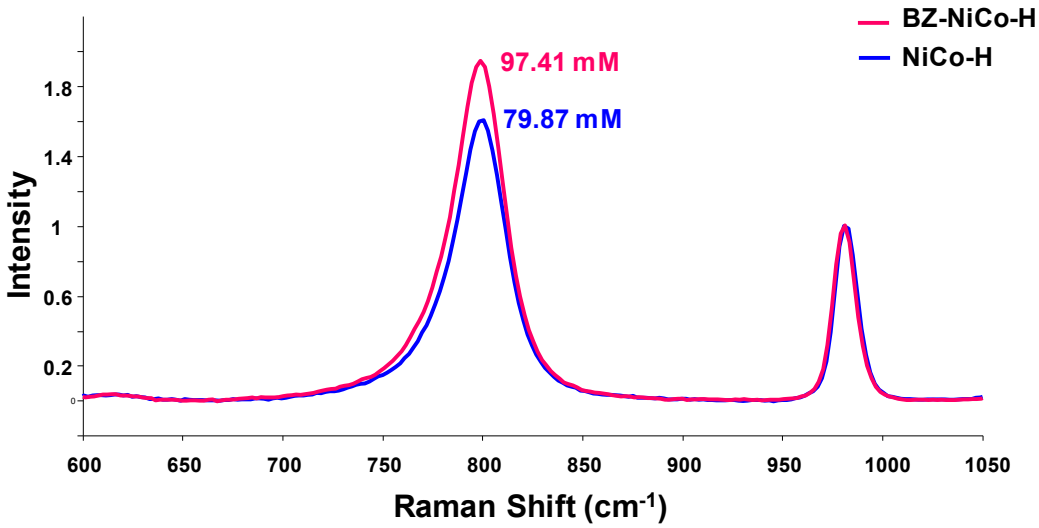

Figure S23. Raman spectra of the electrolyte after 1 h of IOR at 1.60 V vs RHE using BZ-NiCo-H and NiCo-H catalysts, showing higher iodate concentration with BZ-NiCo-H catalyst.

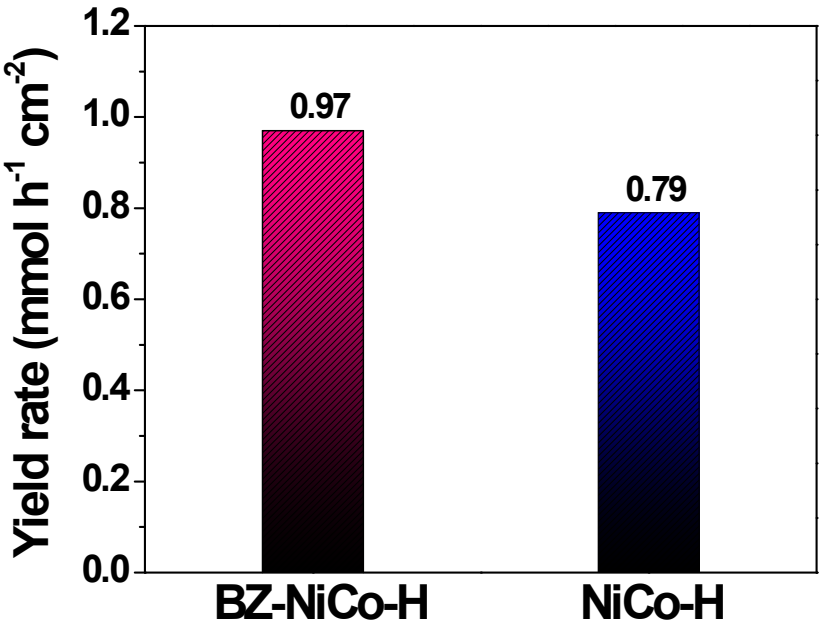

Figure S24. Iodate yield rate of the synthesized catalysts at 1.60 V vs RHE potential.

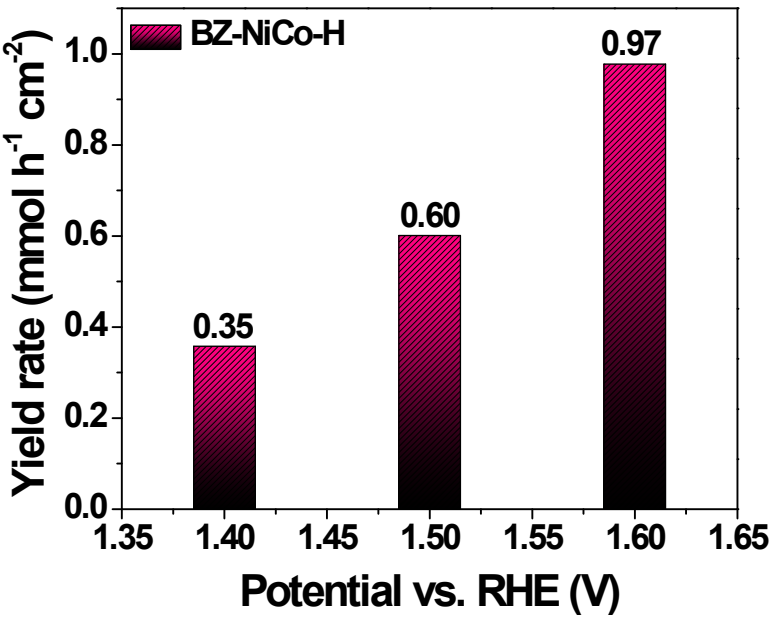

Figure S25. Iodate yield rate at different potentials using BZ-NiCo-H catalyst.

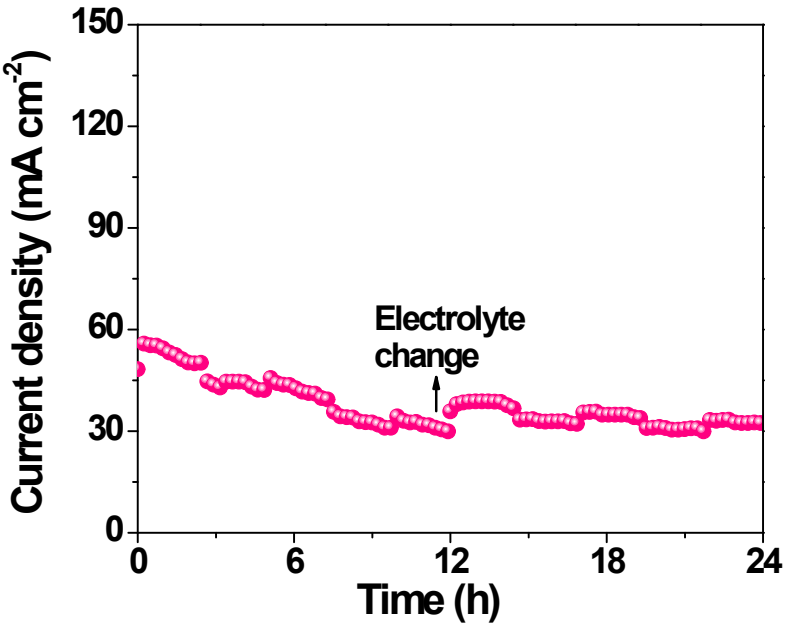

Figure S26. CA stability test of BZ-NiCo-H in 1.0 M KOH containing 0.33 M KI at the potential of 1.50 V vs RHE.

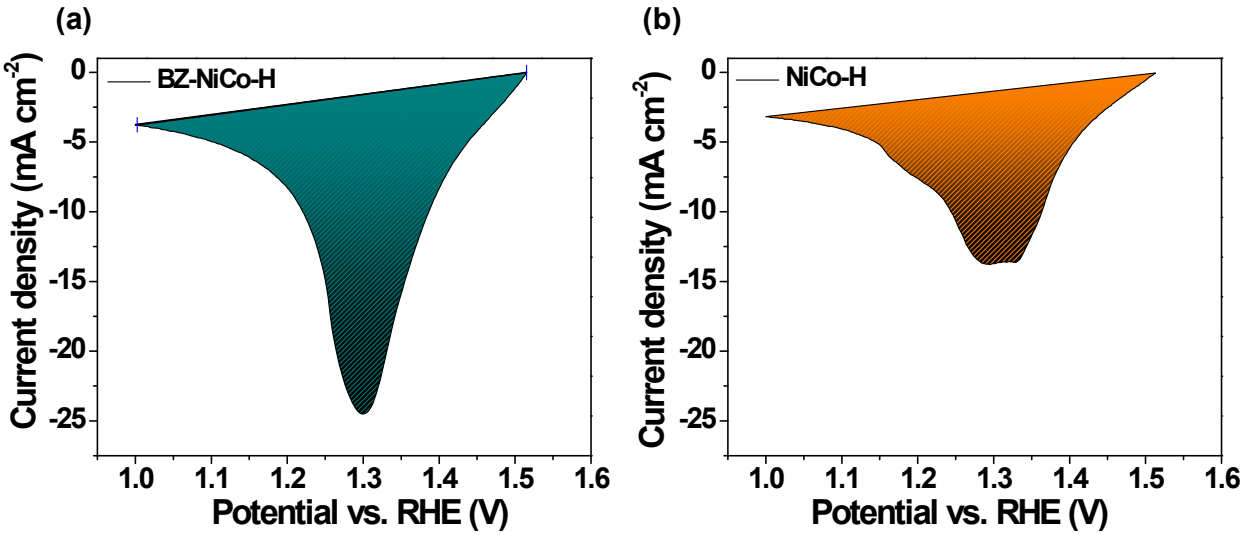

Figure S27. Reduction peak area utilized for integration to determine the number of active sites of (a) BZ-NiCo-H, and (b) NiCo-H.

Determination of surface-active Ni-sites [8]

For BZ-NiCo-H

Calculated area associated with the reduction peak = 3.77×10^{-3} V A

Hence the associated charge is = 3.77×10^{-3} V A / 0.005 V s^{-1}

$= 754 \times 10^{-3}$ A s

$= 754 \times 10^{-3}$ C

Now, the number of electron transferred is = 754×10^{-3} C / 1.60×10^{-19} C

$= 47.12 \times 10^{17}$

Since the oxidation of Ni^{2+} to Ni^{3+} is a single-electron transfer reaction, the number of electrons calculated above is the same as the number of surface-active sites.

Hence, the surface-active Ni^{3+} sites are = **47.12×10^{17}**

For NiCo-H

Calculated area associated with the reduction peak = 2.53×10^{-3} V A

Hence the associated charge is = 2.53×10^{-3} V A / 0.005 V s^{-1}

$= 506 \times 10^{-3}$ A s

$= 506 \times 10^{-3}$ C

Now, the number of electron transferred is = 506×10^{-3} C / 1.60×10^{-19} C

$= 31.62 \times 10^{17}$

The surface-active Ni^{3+} sites are = **31.62×10^{17}**

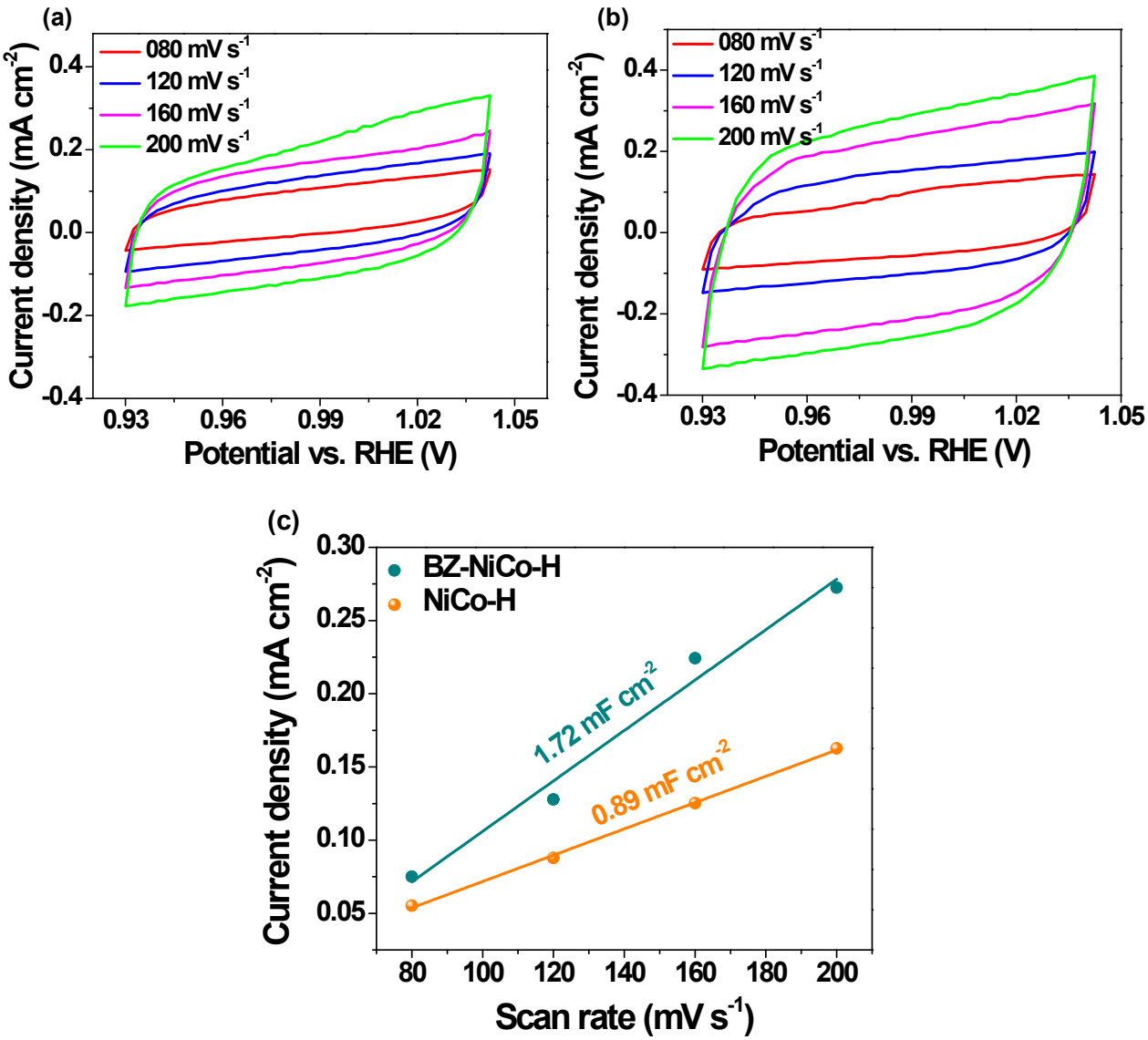

Figure S28. Electrochemical capacitance current of (a) NiCo-H, (b) BZ-NiCo-H, and (c) double-layer capacitance plot of NiCo-H and BZ-NiCo-H.[9]

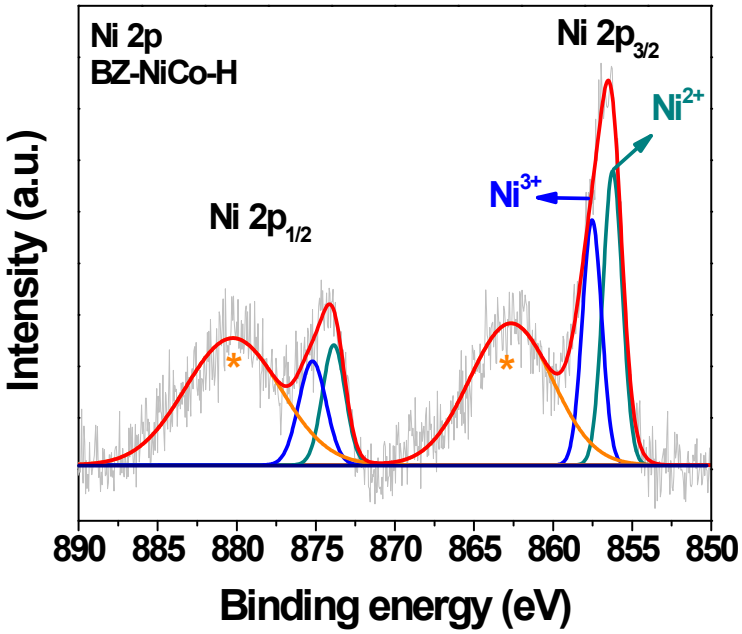

Figure S29. Ni 2p XPS spectrum of BZ-NiCo-H after catalysis, showing positive shift of Ni $2p_{3/2}$ peak by 0.22 eV compared to fresh BZ-NiCo-H.[10-11]

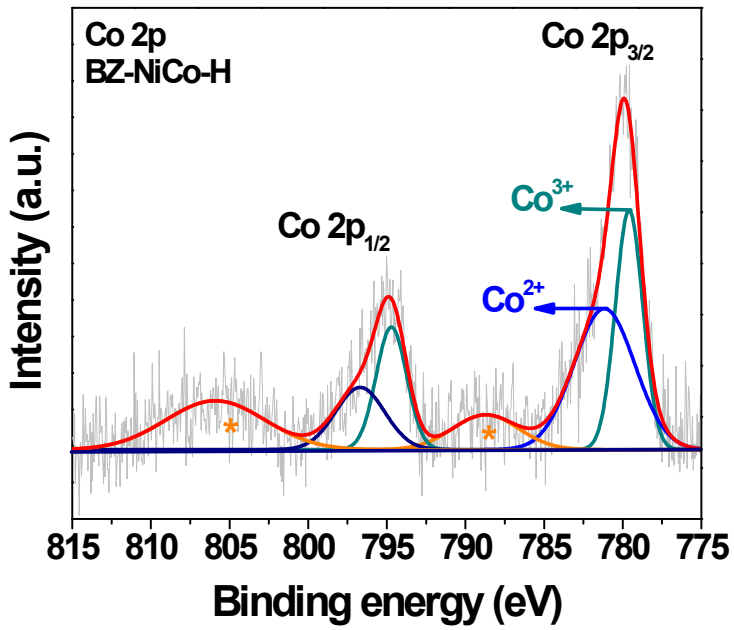

Figure S30. Co 2p XPS spectrum of BZ-NiCo-H after catalysis. The spectrum exhibited two prominent peaks corresponding to Co $2p_{3/2}$ and Co $2p_{1/2}$, with deconvolution of the Co $2p_{3/2}$ peak, revealing two signals at 781.16 eV and 779.62 eV for the Co^{2+} and Co^{3+} species respectively.[12-13]

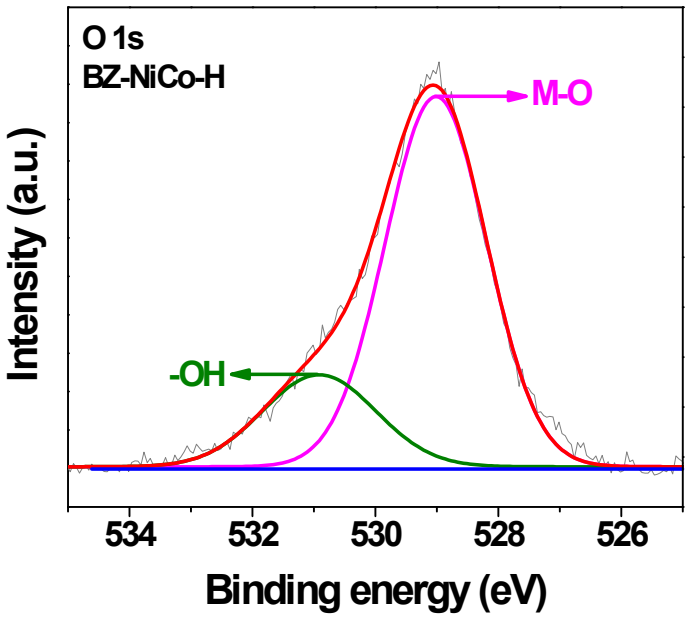

Figure S31. O 1s XPS spectrum of BZ-NiCo-H after catalysis, showing signals for metal-oxygen bond at and surface hydroxyl groups at 529.01 eV and 530.92 eV.[4,7]

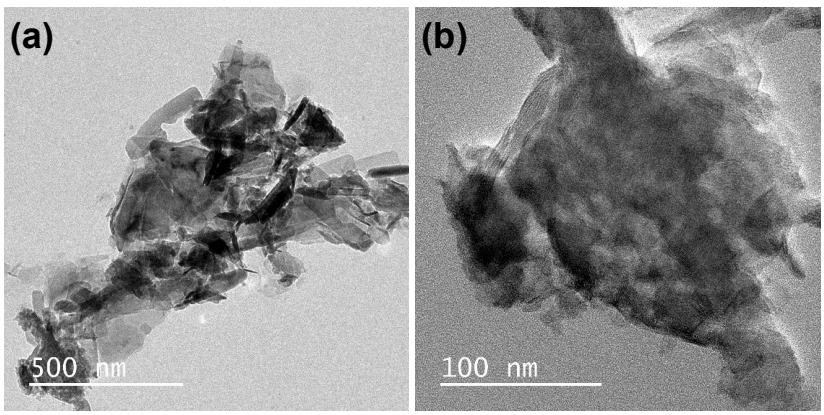

Figure S32. (a,b) TEM images of BZ-NiCo-H after catalysis, showing the ultrathin nanosheets.

References

1 P. Arora, K. Bhadauriya, L. Singh, A. Goyal, S. Verma, B. Singh, A. Draksharapu, *Inorg. Chem.,* 2025, **64**, 5069–5076.

2 M. Ma, R. Ge, X. Ji, X. Ren, Z. Liu, A. M. Asiri, X. Sun, *ACS Sustain. Chem. Eng.*, 2017, **5**, 9625–9629.

3 W. Liu, D. Zheng, T. Deng, Q. Chen, C. Zhu, C. Pei, H. Li, F. Wu, W. Shi, S.-W. Yang, Y. Zhu, X. Cao, *Angew. Chem. Int. Ed.*, 2021, **60**, 10614–10619.

4 A. Goyal, S. Verma, L. Singh, B. Singh, A. Draksharapu, *Chem. Commun.*, 2025, **61**, 6823–6826.

5 S. S. Roy, R. K. Sharma, A. Karmakar, S. Nagappan, B. Pathak, S. Kundu, *Appl. Catal.* B, 2025, **371**, 125227.

6 R. Arulraj, K. Eswaran, S. F. C. M., R. Murugesan, S. Peters, A. Maruthapillai, S. Vadivel, R. K. Konidena, T. Sadhukhan, A. Sengeni, *Chem. Commun.*, 2024, **60**, 4435–4438.

7 B. Singh, R. Kumar, N. Verma, A. Draksharapu, *ACS Appl. Mater. Interfaces*, 2025, **17**, 5008–5016.

8 S. Anantharaj, S. R. Ede, K. Karthick, S. Sam Sankar, K. Sangeetha, P. E. Karthik, S. Kundu, *Energy Environ. Sci.*, 2018, **11**, 744–771.

9 S. Verma, L. Singh, A. Goyal, B. Singh, A. Draksharapu, *ACS Appl. Nano Mater.*, 2025, **8**, 13522–13531.

10 K. Wu, C. Lyu, J. Cheng, Z. Guo, H. Li, X. Zhu, W.-M. Lau, J. Zheng, *Small*, 2024, **20**, 2304390.

11 K. Wu, C. Cao, K. Li, C. Lyu, J. Cheng, H. Li, P. Hu, J. Wu, W.-M. Lau, X. Zhu, P. Qian, J. Zheng, *Chem. Eng. J*., 2023, **452**, 139527.

12 K. Wu, C. Wang, X. Lang, J. Cheng, H. Wu, C. Lyu, W.-M. Lau, Z. Liang, X. Zhu, J. Zheng, *J. Colloid Interface Sci*., 2024, **654**, 1040-1053.

13 X. Wang, S. Huo, Y. Chen, M. Wang, Y. Dai, J. Zou, *Adv. Funct. Mater.*, 2025, **35**, 2506077.